Energy & Buildings 262 (2022) 112002

Contents lists available at ScienceDirect

Energy & Buildings

journal homepage: www.elsevier.com/locate/enb

Field validation of data-driven BSDF and peak extraction models for light-scattering fabric shades

Taoning Wang [a,*], Eleanor S. Lee [a], Gregory J. Ward [b], Tammie Yu [a]

[a] Building Technologies and Urban Systems Division, Energy Technologies Area, Lawrence Berkeley National Laboratory (LBNL), Mailstop 90-3147, 1 Cyclotron Road, Berkeley, CA 94720, USA
[b] Anyhere Software, 950 Creston Road, Berkeley, CA 94708, USA

ARTICLE INFO

Article history:
Received 29 October 2021
Revised 17 February 2022
Accepted 2 March 2022
Available online 4 March 2022

Keywords:
Bidirectional scattering distribution function
Daylighting
Complex fenestration systems
Fabrics
Textiles
Windows
Building energy efficiency
Discomfort glare

ABSTRACT

Shading and daylighting systems affect cooling, heating, and lighting energy use by modulating solar radiation through the building façade. Characterizing shading systems holistically and accurately helps designers and engineers evaluate shading systems to achieve energy and non-energy performance goals. These complex fenestration systems can be modeled using Bidirectional Scattering Distribution Functions (BSDF), which map incident radiation to hemispherical distributions of outgoing radiation. Data-driven, tabulated BSDFs are derived from interpolated goniophotometer measured data, then sampled during the raytracing calculation. A peak extraction (PE) algorithm was developed to circumvent limits in BSDF angular resolution, where the specular peak is extracted during simulation by evaluating the BSDF in the through direction and surrounding region. The objective of this study was to validate this measurement and modeling workflow using field monitored data from a full scale testbed with eleven installed fabrics of different weaves, openness factors, and colors and assess the accuracy of the workflow under different adaptation and contrast conditions. Test conditions were limited to clear sky conditions with the sun in the field of view. Results showed that, for tensor tree datasets, vertical illuminance, solar luminance (2.5° apex), and daylight glare probability (DGP) were predicted to within a mean bias error (MBE) error of −456 lx (−12.3%), −3.46e5 (−38.4%), and −0.042 (−7.8%) when full PE occurred. With a binary classification of glare/ no glare, DGP was predicted accurately with a true positive rate of 0.98 and true negative rate of 1.0 using tensor tree data and less accurately with Klems BSDF data, particularly for cases of no glare. The workflow may be of insufficient accuracy to distinguish borderline performance between fabrics using the four-point glare scale, particularly under low adaptation, high contrast daylit conditions. Errors were due to reductions in peak shape and intensity across the BSDF interpolation and data reduction workflow. Future work is needed to better preserve measurement fidelity during interpolation and sampling, which in turn will improve PE performance.

1. Introduction

Shading and daylighting systems such as Venetian blinds, fabric roller shades, perforated metal, and brise soleil mitigate the effects of solar radiation in and around buildings, thereby affecting thermal and lighting energy use in buildings and associated greenhouse gas emissions [1–5]. Other aspects of building performance are also affected: visual and thermal comfort, view to the outdoors, privacy, and related physiological and psychological effects associated with non-visual effects of daylight [6,7]. Over the past thirty years, considerable research has been conducted worldwide to characterize the solar-optical scattering behavior of shading and daylighting systems [8–11]. Such data are critical for building performance evaluations related to fenestration, enabling quantitative and qualitative analysis of building designs, fair rating and certification of consumer products, and development of innovative technologies [12,13].

Solar-optical "scattering" is characterized using bi-directional scattering distribution functions (BSDF), which describe for any arbitrary incident angle the distribution of outgoing radiation as a result of reflection or transmission through the shading system [14]. BSDFs are derived from measured data, and for some macroscopic systems, by a geometrical description of the system [15]. *Data-driven* BSDFs are based on comprehensive angle-dependent measured data from scanning or imaging goniophotometers [16,17]. With either type of instrument, transmission and reflection measurements are taken of the sample material for a wide

* Corresponding author.
E-mail address: taoningwang@lbl.gov (T. Wang).

https://doi.org/10.1016/j.enbuild.2022.112002
0378-7788/

range of incident and exiting angles, fit with an interpolant, and reduced to a tabulated representation (e.g., Klems 145x145 matrix [10]). The tabulated data are then used in Radiance [18] ray tracing and matrix algebraic simulations [19–24] to compute climate-based solar irradiance and photometric (i.e., illuminance, luminance) quantities, and for physically-based renderings. Data-driven BSDFs have the distinct advantage of being generated strictly from measured data without use of any fitting parameters specific to a particular class of shading system. Analytical BSDFs, on the other hand, are continuous functions based on physics-based models of specific materials (e.g., glass) or regression models derived from empirical data [25,26]. These BSDFs can be used directly for renderings or represented with tabulated representations for matrix-based simulations.

Early research involving matrix-based simulations identified shortcomings in accuracy due to insufficient angular resolution of the BSDF hemispherical basis, particularly for shading and daylighting systems that exhibit specular and diffuse transmission and reflection characteristics [27]. These low-resolution BSDFs simply lumped the scattering distribution's flat regions and peaks into a large solid angle, which is sufficient for solar heat gain calculations but insufficient for daylight metrics requiring detailed spatial evaluations of contrast (e.g., discomfort glare and view). Introduction of variable-resolution BSDF bases and alternate matrix-based methods solved this problem in part by calculating the diffuse component separately from the direct sun component [20,28,29]. Sensitivity analysis illustrated the significance of this problem [30].

Further field validation, however, pointed to additional limitations with the method, particularly with respect to glare and vertical illuminance (i.e., a quantity of importance for circadian entrainment) [31,32]. In response to underestimated solar luminance seen through forward scattering and specular transmitting materials, Geisler-Moroder et al. developed a peak extraction (PE) algorithm that tested for specular transmission and, if present, modified the flux assigned to the solar orb and circumsolar region [33]. The workflow from scanning goniophotometer measurements to the final rendered image was validated with comparisons of simulated data to field measured data for a single case study of a low transmittance, dark-colored fabric shade [16]. This work demonstrated how the PE algorithm increased the modeling accuracy of forward scattered luminous flux compared to existing methods.

In this study, we extended the prior field validation to verify that the workflow and PE method are reliable and sufficiently accurate across a broad range of forward scattering, specular transmitting, roller shade fabrics; i.e., a) conserves total energy over a range of solar conditions, and b) models specular transmitted flux to a sufficient degree of accuracy. The models and workflow were identical to the prior validation study except for minor adjustments to the PE algorithm and sampling parameters (described in Section 2.4.2). Illuminance and luminance data for eleven fabrics ranging from light to dark gray and openness factors from 1% to 5% were collected in a full-scale outdoor testbed and compared to simulations of vertical illuminance, source luminance, and discomfort glare. Conclusions from this study are limited to fabric/ textile shading materials that transmit radiation with a specular (through) component with varying degrees of forward scattering.

2. Method

2.1. Description of shading materials

Eleven manufactured roller shade fabrics were selected for the study, spanning a range in solar protection and daylight admission (Table 1). All fabrics were woven with single- or multi-color opaque polyester yarns or polyester yarns encapsulated in a PVC coating with a total shade thickness of 0.737 mm. There were two types of weaves (basket and twill, Fig. 1), two colors (light and dark shades of white to dark grey), and three openness factors (OF, 1%, 3%, and 5%). All three properties contributed to variable qualities of specular transmission and forward scattering. In the subsequent sections, each fabric is labeled by weave, color, and OF; e.g., BL1 = B (asket) L(ight color) 1(% OF). The two types of twill weave fabrics are distinguished by an apostrophe ('). T' denotes twill weave fabrics made of 100% polyester threads, whereas T denotes twill weave fabrics made of 70% PVC and 30% polyester.

2.2. Characterization with scanning goniophotometer measurements

Visible light properties of the fabrics were measured using a scanning goniophotometer (Model "pgII," Pab Advanced Technologies Ltd [34–36]), which is capable of measuring intensities within a dynamic range of 70 dB. For each incident angle, more than 1e5 directions were sampled in each hemisphere. In this study, the source was focused on the detector such that the sample illumination area was approximately 20 mm in diameter. Incident angles selected for the pgII measurements and assumed symmetry for each fabric are summarized in Table 2. Direct-diffuse and direct-hemispherical transmittance and reflectance measurements of seven of the fabrics were made at normal incidence with a Perkin-Elmer Lambda 950 spectrophotometer equipped with a 150 mm integrating sphere.

Table 2 and Fig. 2 provide the normal incidence hemispherical and specular transmission (over a 10° apex angle) based on Delau-

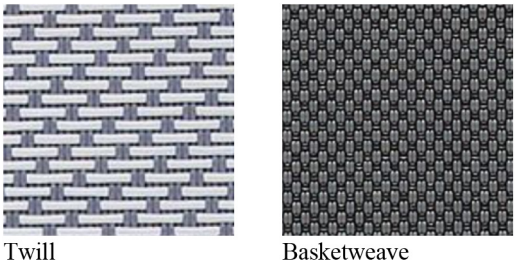

Fig. 1. Example twill and basket weave patterns, demonstrating 180° rotational and quadrilateral symmetry, respectively. See Figure A2 in [16] for symmetry definitions.

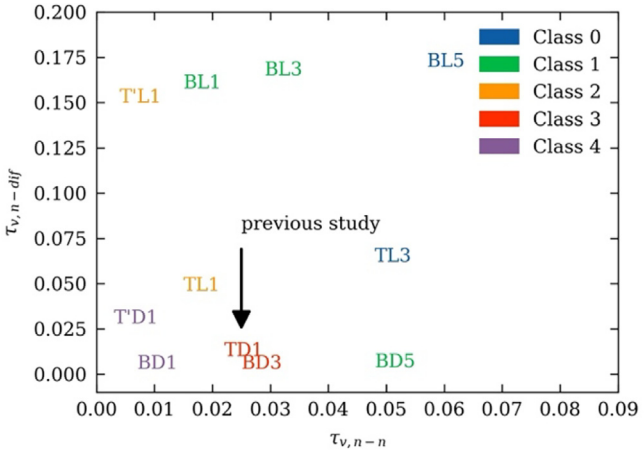

Fig. 2. Measured fabrics' normal-normal and normal-diffuse transmittance. The colored legend indicates the glare control classification given in Table E.3 of the EN 17037 Standard and Table 7 of EN 14501, where Class 0 has very little effect and Class 4 has very good effect on control of discomfort glare.

Table 1
Description of roller shade fabrics.

Fabric No.	Label	Weave	Color	Openness factor (%)	Direct view through fabric?
1101	BL1	Basket	White	1%	No
1601	BL3			3%	Yes
1901	BL5			5%	Yes
1112	BD1	Basket	Charcoal	1%	Yes
1612	BD3			3%	Yes
1912	BD5			5%	Yes
6858	T˙L1	Twill	Titanium	1%	Yes
6206	TL1	Twill	Silver	1%	Yes
6006	TL3			3%	Yes
6857	T˙D1	Twill	Timber	1%	Yes
6216	TD1	Twill	Slate	1%	Yes

Table 2
Scanning goniophotometer measurement conditions and summary transmission data.

Fabric	$\tau_{v,n\text{-}h}$	$\tau_{v,n\text{-}n}$	$\tau_{v,n\text{-}dif}$	Incident phi (°)*	Assumed symmetry
BL1	0.173	0.015	0.158	0°-90°	Quad
BL3	0.194	0.029	0.165	0°-90°	Quad
BL5	0.227	0.057	0.170	0°-90°	Quad
BD1	0.010	0.007	0.003	0°-90°	Quad
BD3	0.028	0.025	0.003	0°-90°	Quad
BD5	0.052	0.048	0.004	0°-90°	Quad
T˙L1	0.154	0.004	0.150	0°-180°	180° Rotational
TL1	0.061	0.015	0.046	0°-90°	Quad
TL3	0.110	0.048	0.062	0°-90°	Quad
T˙D1	0.031	0.003	0.028	0°-180°	180° Rotational
TD1	0.032	0.022	0.010	0°-330°	180° Rotational

Notes: Quad = quadrilateral symmetry; $\tau_{v,n\text{-}h}$ = hemispherical visible transmittance at normal incidence; $\tau_{v,n\text{-}n}$ = direct normal visible transmittance at normal incidence.
* incident theta angles were: 0, 10, 20, 30, 40, 50, 60, 70, 82.5, 97.5, 110, 120, 130, 140, 150, 160, 170, and 180°; phi angle steps were 45° at 10° theta, 22.5° at 20° and 30° theta, and 15° at 40° theta towards grazing. All phi and theta angles in this report are given using the Radiance convention [16].

nay triangulation of measurement points. These data were output from *Mountain*, the software provided with the pgII instrument, and were confirmed to agree with integrating sphere data to within 4.4%. Fig. 2 also shows the level of glare protection provided by each of the shades as defined by the EN 14501 Standard.

2.3. Field measurements with HDR imaging system

Field measurements were conducted in the Advanced Windows Testbed, an outdoor, full-scale, side-lit testbed at the Lawrence Berkeley National Laboratory, Berkeley, California (37.87°N, 122.27°W). Measurements were performed in each of three, side-by-side, private office test chambers under clear sky conditions from November 2–30 when the sun was in the field of view of the camera. Each chamber was 3.05 m by 3.05 m by 4.57 m in width, height, and depth with a south-facing window (2.75 m × 2.75 m). A different fabric was installed in each chamber, where the shade fabric was mounted to cover the entire window. The electric lighting was turned off.

Window luminance measurements were made 1.0–1.5 m from the window, facing normal to the window (Fig. 3). Measurements were made using a high dynamic range (HDR) imaging system consisting of a full-frame, digital single-lens reflex camera (Canon 5D), and a 180° fisheye lens (Sigma 8 mm). Different neutral density filters (i.e., filters 87.5%, 99%, or 99.9% of visible light) were applied, per fabric, to the backside of the lens to increase the measurable luminance range and avoid pixel overflow for the shortest exposure (1/8000 s), as required per fabric type. Sequences of low dynamic range (LDR) images (3840 × 5760 pixels) were taken in the RAW format and then combined to generate HDR images (2000 × 2000 pixels). Fisheye images were remapped from equisolid-angle to equidistant projection. Lens vignetting was corrected for each aperture setting. Each HDR image was then calibrated using a separate spot luminance meter reading (Minolta LS110, 0.5° spot), aimed at the fabric's 5 cm by 5 cm cutout. Two layers of diffusing mylar sheet covered the cutout. The cutout with mylar sheets provided a bright target, at around 5e3 cd/m^2, for the luminance meter. Vertical illuminance was measured within 7 cm of the center of the fisheye camera lens using a cosine corrected, v (Lambda) weighted, photometric sensor (Minolta T10, within 6% of v(Lambda) and 3% of cosine response over 0.01–299,900 lx range). Agreement between the photometric reference sensor and HDR sensor (Fig. 4) readings of vertical illuminance was within a root mean square error (RMSE) of 275 lx and mean bias error (MBE) of −163 lx (−4.36%).

Fig. 3. Left: HDR imaging system. Right: Imaging system located in the testbed.

Direct normal and diffuse horizontal irradiance were measured at the full-scale testbed using a pyrheliometer (EKO MS-80, <0.2%

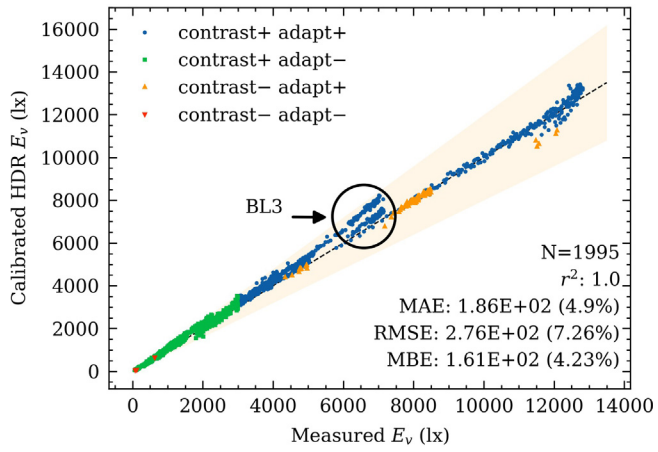

Fig. 4. Measured vertical illuminance, E_v (lx), of photometric sensor (x-axis) versus HDR sensor (y-axis) for all measured conditions. The colored legend depicts measured data per saturation and contrast glare categories defined in Section 2.5. Data within the circle are for fabric BL3.

non-linearity at 1000 W/m^2, spectral error ± 2%) and pyranometer (EKO MS-57, <0.2% non-linearity at 1000 W/m^2, spectral error ± 2%) mounted on a solar tracker. For the validation, data points were culled when the solar disk and circumsolar area (within an approximate apex angle of 5°) were obstructed by the window mullion. Data points where the HDR vertical illuminance deviated from the illuminance sensor more than 20% were also culled. These included points when either of the two sensors was shaded by the window mullion. Angles of incidence for all measured fabrics are given in Fig. 5.

2.4. Simulation using tabulated BSDF data

2.4.1. Generating tabulated BSDF data for simulation

Tabulated data-driven BSDF data, in the tensor tree and Klems format, were derived from pgII measurements in two stages:.

1) Produce scattering interpolants from goniophotometer measurements, then
2) Produce the tabulated BSDF by sampling the scattering interpolant.

The Radiance tool *pabopto2bsdf* [37] was used in the first stage to produce the scattering interpolants. For this study, measured pgII data points were discarded for angles of incidence where theta was greater than 80° (front side) and<100° (backside). Data for these very low grazing angles were noisy and exceeded the angular limits of the pgII. For fabrics assumed to have 180° rotational symmetry (fabrics that look the same when rotating 180° in-plane), the *-s u2* option of *pabtopto2bsdf* was used, which copied pgII data points with incident phi spanning 0–180° to cover 180–360°, treating the entire BSDF dataset as anisotropic. The Radiance tools *bsdf2ttree* and *bsdf2klems* were used to sample the scattering interpolants to produce the tabulated tensor tree and Klems BSDF. The tabulated tensor tree BSDF was generated using the 4096 × 4096 hemispherical basis resolution (anisotropic, generation six, 95% culling) with a minimum (smallest) angular resolution of 2.53°.

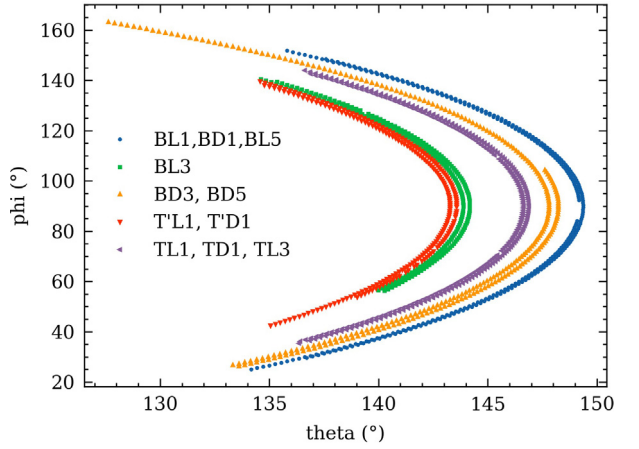

Fig. 5. Incident solar theta and phi angles per fabric type over the field test measurement period.

2.4.2. Simulation using peak extraction algorithm

Daylight simulations were performed using the Radiance aBSDF material type to invoke peak extraction. During peak extraction, 29 directions are sampled over a regular grid covering a search radius of roughly three times the minimum resolution about the center, and the BSDF values are then sorted in descending order. This sampling ensures that a peak will be found in the vicinity of the true "through" direction. Each sample in the list is added to the peak if its solid angle matches the smallest associated with the tabulated BSDF, and the accumulated peak average is not more than eight times the considered sample. After the peak is thus determined, the direct transmission (i.e., average peak times solid angle) must be greater than 0.05% to finally be extracted and used for PE. This threshold was determined empirically from the testing of many BSDFs. If a peak is detected in this radius, an exclusion zone is created with a size based on the BSDF resolution and source size. Solar luminance (e.g., sun luminance at the eye) is then modeled by multiplying the source luminance by the integrated direct transmission in that direction. This intensity is assigned to the solid angle of the sun (0.53°). The surrounding exclusion zone, defined by the initial 29 samples, has an average luminance based on the average BSDF in the area just outside the peak. Peak extraction is partially triggered when the exclusion zone is established but the algorithm decides the peak in the tabulated BSDF is not pronounced enough to be a specular peak. Peak extraction is completely triggered when both the exclusion zone and specular peak are identified [16]. Parameters used in the peak detection code were developed and tested using clear glass[1], fabrics, translucent materials, and redirecting venetian blinds. After the initial validation [37], minor adjustments to the PE algorithm and sampling parameters were made due to small errors detected in this study. Specifically, the peak sampling radius and number of samples were increased, and recovery of energy in the surround was introduced [33].

To determine whether PE should be applied, visual inspections were made of each fabric. The choice to turn on or off peak extraction was based on whether one can see through the sample and distinguish the objects on the other side from a distance of 2 m from the sample. By visual inspection, all fabrics except BL1 had a direct view component (Table 1). Thus, all fabrics except BL1 were modeled using the Radiance *aBSDF* material type, turning on peak extraction, whereas BL1 was modeled using the regular BSDF material type. If *aBSDF* is used for system with a non-through component, PE can potentially be triggered, resulting in significant overestimation in the through component.

[1] Simulations of clear glass were conducted using an analytic model versus Klems and anisotropic tensor tree BSDFs with PE. BSDF-derived source luminance levels for a constellation of six 1.5° diameter suns were within 1–2% of the analytic-derived, gold standard values. The PE detection code should be robust to different BTDFs, but as with any approximation, there will be corner cases that are handled less well.

The Radiance *rtrace* program was used to produce vertical illuminance data (at 2 min intervals) and HDR renderings (at 10 min intervals) from which luminance data were derived.[2] Skies were modeled with the continuous Perez all-weather sky model using site-measured direct normal and diffuse horizontal irradiance at 1 min timesteps. HDR images were rendered using an equiangular fisheye projection at 2000 × 2000 pixel resolution, matching the measured HDR image properties. For HDR images where peak extraction was invoked, the solar disk in those images was rendered with a 0.533° apex angle, then blurred based on the human retinal blurring function which also approximated the blurring effect of the camera lens [16]. The simulated blurred solar disk matched the HDR measured solar disk shape such that both had a full width tenth maximum of approximately 0.75°.

Measured and simulated HDR images were evaluated using the *evalglare* program [38] with the following settings: no task area defined, regular glare source detected at 2000 cd/m^2, peak glare source ($L_{s,e}$) separately extracted at 5.0e4 cd/m^2. For each input HDR image, *evalglare* computes, among other outputs, daylight glare probability (DGP) [39], vertical illuminance, glare source luminance, solid angle, and × and y pixel location for each glare source. With the peak source pixels at the center, luminance values were also extracted from the sun orb and circumsolar region at apex angles of 0.53° and 2.5° using *evalglare* with the *-l* option.

2.5. Measured HDR images by adaptation and contrast levels

Measured data were first sorted into two categories of discomfort glare: saturation and contrast glare. Saturation glare is dictated by the overall illuminance at the eye while contrast glare is caused by high-intensity glare sources within the field of view in a dimly lit scene. Measured HDR images were sorted by two levels of adaptation (i.e., low versus high vertical illuminance) and two contrast levels. The dividing point between low and high adaptation levels was E_v = 3000 lx because it is the vertical illuminance level that causes just noticeable discomfort glare (DGP = 0.34) without any contrast in the scene [40]. Data were then sorted based on contrast, where the contrast level was defined by the log_gc term from the DGP Eq. (1) below (second term without the coefficient). The dividing point in log_gc between high and low contrast was set at 0.5, which contributes 0.046 to DGP or approximately an increase of a glare category [41]. The resultant four glare categories were labeled with the notation: adapt + or adapt- and contrast + or contrast-.

$$DGP = 5.87 * 10^{-5} E_v + 9.18 * 10^{-2} \log_{10}\left(1 + \sum_{i=0}^{n} \frac{L_{s,i}^2 * \omega_{s,i}}{E_v^{1.87} * P_{s,i}^2}\right) + 0.16 \quad (1)$$

3. Results

The eleven tested fabrics exhibited a wide range of hemispherical and specular transmission properties in the visible spectrum. Measured vertical illuminance ranged from 100 lx to 10,000 lx and direct solar transmittance, when evaluated at a 0.53° subtended angle, ranged from about 5e5 to 3e7 cd/m^2. Ten of the eleven fabrics created high contrast conditions, with four at high and six at low adaptation levels (Fig. 6). Because measurements were performed when the sun was in the field of view of the camera, about 95% of the total measured data points for all fabrics were with high contrast conditions. Dark grey colored fabrics exhibited low adaptation levels, while light colored fabrics exhibited high adaption levels, as expected. BL1 with no direct view component produced a low contrast, high adaptation environment. Plots showing results data distributions and tables with errors associated with each dataset can be found in the appendix.

3.1. Energy conservation: $\tau_{v,\ dir\text{-}h}$ and vertical illuminance

Direct-hemispherical visible transmittance ($\tau_{v,dir\text{-}h}$) and reflectance ($\rho_{v,dir\text{-}h}$) for both front and back surfaces were derived from the original pgII data using *Mountain* software (Section 2.2) and from tabulated BSDFs (Section 2.4.1) for all pgII measured incident angles and for all fabrics. Tabulated data were computed using Radiance's *testBSDF* program. Overall, the tabulated tensor tree and Klems data were found to be in good agreement with the original pgII dataset (Fig. 7): the combined mean absolute error (MAE) and RMSE was 4.7% and 8.3% for transmittance and 2.2% and 3.5% for reflectance, respectively. Some combination of the sampling rate differences and noise in the low intensity pgII data most likely explains overall differences. Errors were lower with the Klems dataset (MAE of 2.22%) compared to the tensor tree dataset (4.65%) and were in part due to lower discrepancies at grazing angles. The tensor tree basis loses resolution toward grazing more than the Klems basis because 1) Klems is only a little coarser in theta at grazing whereas the tensor tree uses cos(theta) for its angle steps, and 2) *bsdf2klems*, the tool used to derive the Klems dataset, subdivides its incident angle while sampling, whereas *bsdf2ttree* (tool for tensor tree dataset) does not, so the averaging of *bsdf2ttree* is not quite as good for an equivalent resolution. Fig. 8 illustrates how the tensor tree dataset deviates more from Mountain-derived $\tau_{v,dir\text{-}h}$ values at grazing angles compared to the Klems dataset. Even though pgII data beyond 80° (and 100° on the other side) were discarded when generating tabulated BSDFs, pgII data beyond those theta angles were still used in this comparison.

A total of 2221 vertical illuminance (E_v) data points were collected in the outdoor testbed across the eleven fabrics with a median of 3704 lx. With the tensor tree dataset, MAE, RMSE, and MBE errors for vertical illuminance were 478 lx, 676 lx, and −456 lx, normalizing to 12.9%, 18.2%, and −12.3%, respectively (Fig. 9). For simulations that used the Klems dataset, MAE, RMSE, and MBE errors were lower at 373 lx, 532 lx, and −307 lx, normalizing to 10.1%, 14.4%, and −8.3% respectively. The negative mean bias error indicates an underestimation of E_v. E_v errors were low under low contrast conditions (MBE of −5.5% and −2.1%) and higher under high contrast conditions (MBE of −19.2% and −11.7%) for low and high adaptation levels, respectively. E_v error summary tables are included in the Appendix.

3.2. Energy conservation: Solar luminance

Solar luminance values (Ls) were evaluated for various subtended angles from measured and simulated images to assess energy conservation in the region of specular transmission. The tabulated BSDF resolutions used in this study, both tensor tree and Klems, were too low to preserve solar energy at a 0.53° subtended angle. Thus, accurately predicting solar luminance relied heavily on the performance of peak extraction.[3] When PE was fully triggered, i.e., when a 0.53° subtended solar peak was extracted, the MAE for $L_{s,0.53°}$ for all fabrics tested was 33.1% and 48.1% for the tensor tree and Klems datasets, respectively. Tensor tree datasets

[2] *Rtrace* simulation parameters were the same as those used in the initial validation study [16].

[3] Cases where PE was not used or not triggered are not part of the analysis in this section. Of the eleven fabrics tested, ten fabrics were simulated with peak extraction, where peak extraction was not triggered completely in one of the fabrics (BD1) and inconsistently in another (BD3), indicating absence of a strong specular peak.

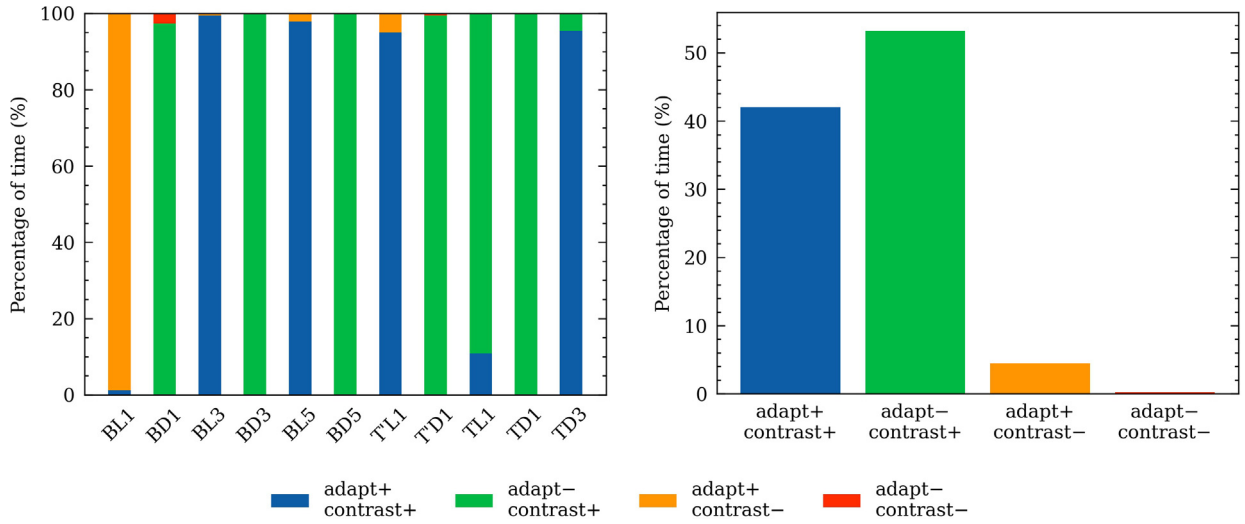

Fig. 6. Percentage of measured HDR images per adaptation and contrast categories for each fabric (left) and for all measured fabrics (right). 95% of the measured HDR images were in the high contrast category.

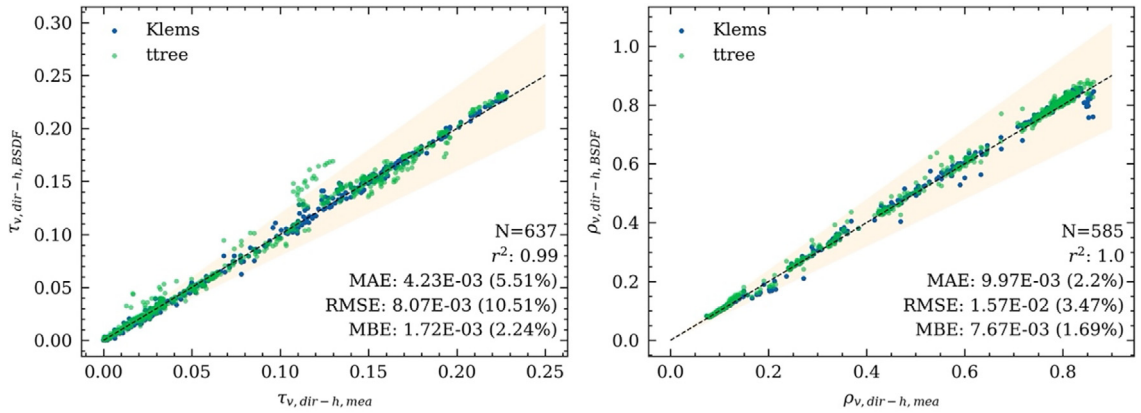

Fig. 7. Direct-hemispherical transmittance ($\tau_{v,\,dir\text{-}h}$) (left) and reflectance ($\rho_{v,\,dir\text{-}h}$) (right) for front and back (outdoor) surfaces from pgII measurements (x-axis) and tabulated Klems or tensor tree BSDF data (y-axis). Statistics are given for Klems and tensor tree data combined. The shaded area denotes an error range of ± 20%. The larger errors occurred at grazing incident angles for all fabrics.

showed better correlation (r^2 = 0.72) with $L_{s,0.53^\circ}$ measurements compared to the Klems datasets (r^2 = 0.34). Similar correlation trends were found when evaluating solar luminance at a 2.5° subtended angle (Fig. 10).

Overall, solar luminance values evaluated at 0.53° and 2.5° subtended angles were significantly underestimated. The majority of data were for high contrast conditions. Among those cases, under high adaptation levels, $L_{s,2.5^\circ}$ was underestimated by −3.33e5 (−32.0%, n = 192) whereas under low adaptation levels, $L_{s,2.5^\circ}$ was underestimated by −3.64e5 (−45.5%, n = 243) for the tensor tree datasets. The corresponding values for the Klems datasets are 1.08e2 (0.01%, n = 192) and −3.82e5 (48.0%, n = 252). Note that tensor tree datasets have higher r^2 = 0.8 as oppose to 0.4 from the Klems datasets, indicating better correlation with measurements. Tables summarizing the errors for tensor tree and Klems datasets are included in the Appendix.

3.3. Glare prediction

The *evalglare* tool uses a unique method based on human factors studies for detecting and identifying glare sources. As a result, its source solid angle and luminance levels differ from the L_s results given in Section 3.2 (L_s was used to assess energy conservation rather than discomfort glare). The MAE for peak source (solar) luminance ($L_{s,e}$; i.e., pixels extracted by *evalglare* at greater than 5e4 cd/m^2) – 3.03e5 cd/m^2 (22.4%) for the tensor tree dataset and 5.43e5 cd/m^2 (40.3%) for the Klems dataset – was an order of magnitude lower than that for the $L_{s,0.53^\circ}$ data. The MBE for $L_{s,e}$ was even lower: +4.72e4 (3.49%) and + 4.40e4 (32.56%) for the tensor tree and Klems dataset, respectively (Fig. 11).

When comparing simulated and measured DGP values, however, we see there is a significant negative bias. This was likely due to the under-predicted E_v and/or solid angle of the glare source, meaning there were more solar disk pixels detected that were greater than 5e4 cd/m^2 from the measured images than from the simulated images. The MBE between measured and simulated peak source solid angle ($\omega_{s,e}$) was −3.73e-4 sr (40.6%) and −3.67E-4 sr (39.9%) for the tensor tree and Klems datasets, respectively. These errors were a result of the PE algorithm which was designed to address the practical angular resolution limits of the goniophotometer and sampling/ computational limits of backwards ray tracing. An in-depth discussion of the effects of measurement limits and representation on $L_{s,e}$ and $\omega_{s,e}$ accuracy is given in [16].

For all datapoints, DGP agreed within a MAE of 0.063 (11.9%) and 0.046 (8.7%) for tensor tree and Klems BSDF datasets, respec-

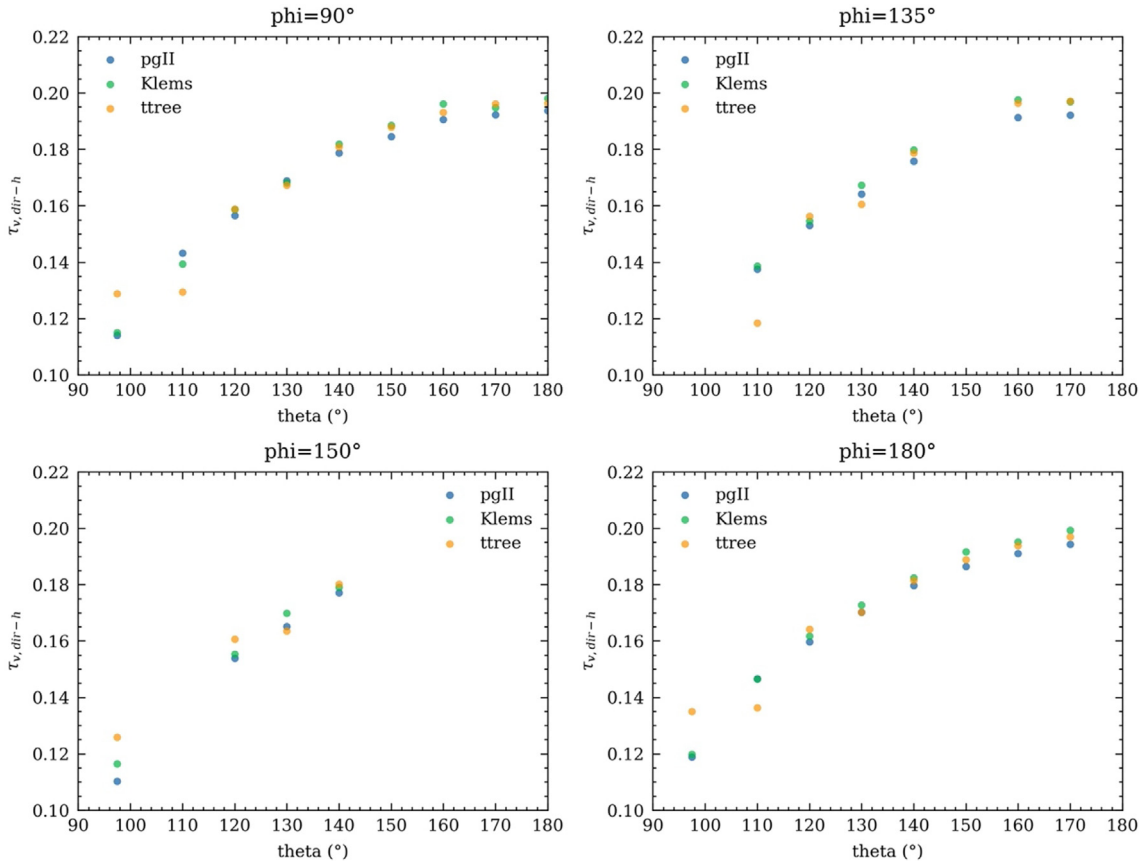

Fig. 8. Direct-hemispherical transmittance ($\tau_{v,\ dir\text{-}h}$) for incident theta (outdoor-facing back surface) and phi angles 90°, 135°, 150°, and 180°. Data given for pgII measured data and corresponding Klems and tensor tree tabulated datasets (measured theta angles differed per phi angle). Fabric BL3. Theta angles were within 133-150° for the field measurements.

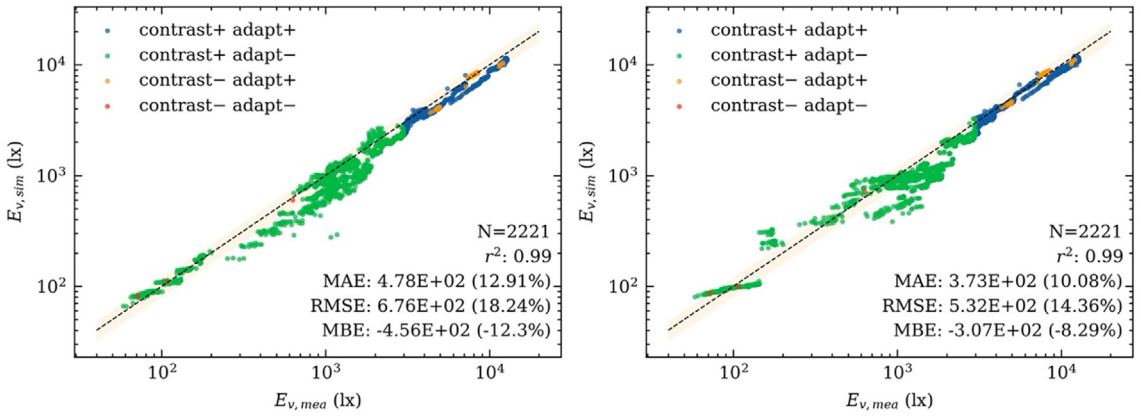

Fig. 9. Measured (x-axis) and simulated (y-axis) vertical illuminance, E_v (lx), for the eleven fabrics. Simulated E_v were generated using the tensor tree (left) and Klems (right) BSDF datasets. The shaded area denotes an error range of ± 20%.

tively. Some of the discrepancies between simulated and measured values under low light conditions were due to peak extraction not being triggered. This resulted in an underestimation of solar luminance, which is critical for predicting DGP. When PE was fully triggered, the DGP MAE error was reduced to 0.044 (8.0%) and 0.035 (6.3%) for the tensor tree and Klems BSDFs, respectively. Note, a DGP error of 0.04 is equivalent to half of a glare category on the four-point[4] discomfort glare scale so under some conditions, the workflow may not be sufficient to differentiate between glare categories.

Using the glare / no-glare, binary classification (DGP greater than 0.38 [40]), however, simulated data were shown to reliably predict discomfort glare with a true positive rate of 0.98 and 0.99, and a true negative rate of 1.0 and 0.26, for the tensor tree and Klems datasets, respectively. A similar trend is shown in Fig. 12, where for measured DGP data points greater than 0.38, almost all (98%) simulated tensor tree data points are also greater than 0.38. The same is true when considering non-glare cases (i.e., DGP $\leq$ 0.38). For the Klems dataset, 11 out of the 43 simulated dat-

[4] The four-point glare rating scale [48] is defined by subjective responses to glare: "imperceptible," "noticeable," "disturbing," and "intolerable.".

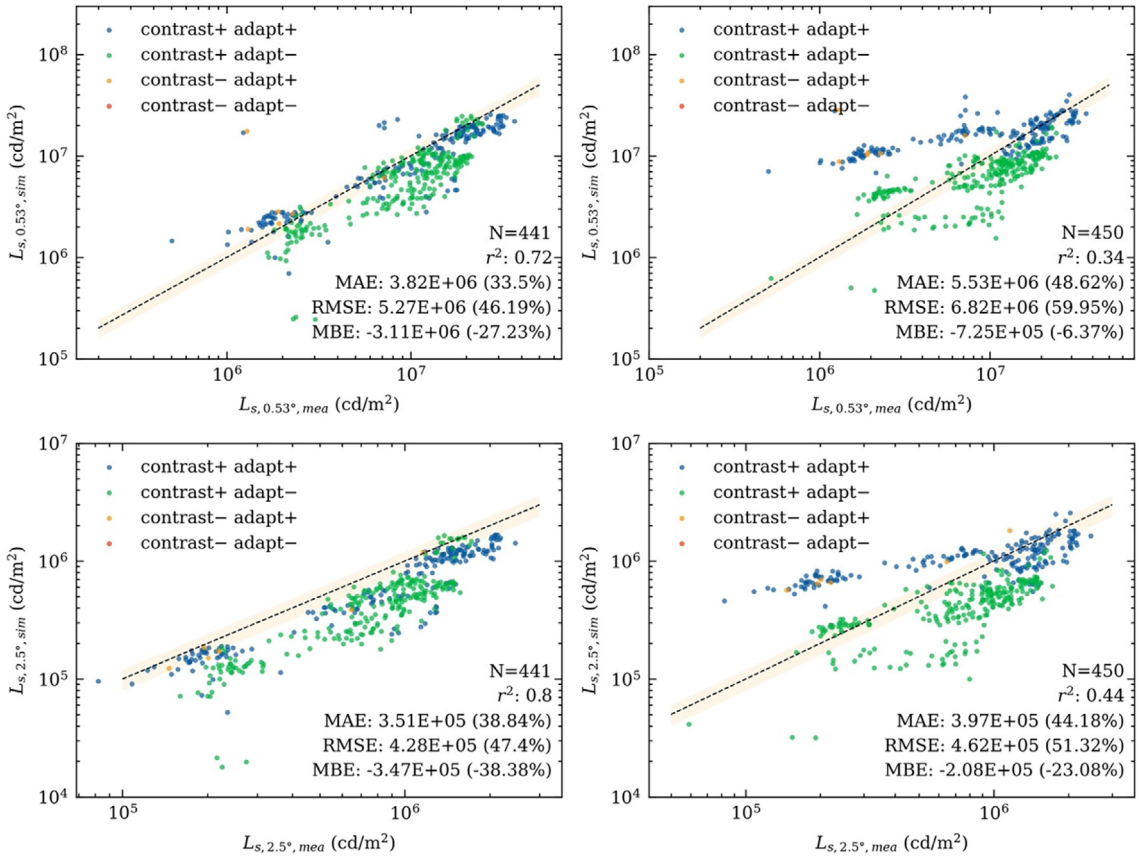

Fig. 10. Measured (x-axis) and simulated (y-axis) solar luminance, L_s (cd/m^2), evaluated for 0.53° (upper plots) and 2.5° (lower plots) subtended angles. Simulated values were based on tensor tree (left) or Klems (right) tabulated BSDF. Data given for when full PE occurred. The shaded area denotes an error range of ± 20%.

apoints agreed with measured DGP for non-glare cases. Fig. 12 (right) shows the distribution of all measured data points in terms of log_gc (contrast) and E_v (adaptation). This plot shows that all high adaptation data points (E_v greater than 3000 lx) are in the glare category while low adaptation and high contrast data points span glare and no-glare category. The low E_v (around 200 lx) and high log_gc cases shown in Fig. 12 (right) are from fabric BD1, which produced extremely low adaptation levels and high contrast.

We provide a summary of errors for all simulated tensor tree data and two subset datasets where PE was fully triggered and where PE was fully triggered and DGP was<0.6 (top three sets of bars in Fig. 13). As noted above, the predictive accuracy for $L_{s,e}$, $\omega_{s,e}$, and DGP improves when fabrics with a weak specular component are excluded from the "All" dataset, i.e. where PE is fully triggered. With weak specular transmission, the prediction is wholly reliant on the tabulated BSDF data with its limited resolution.

The lower four sets of bars in Fig. 13 subdivide all simulated data where PE was fully triggered into the four glare categories based on contrast and adaptation level. In cases with high contrast, the DGP MAE are 0.067 and 0.029 for the high and low adaptation levels. In cases with low contrast and high adaptation, the MAE is 0.011 (n = 6). There were no data points with low contrast and low adaptation where PE was fully triggered. Tables summarizing the errors are included in the Appendix.

4. Discussion

4.1. Sources of error across the simulation workflow

Further validation with a broader range of scattering materials confirmed many of the trends identified in the pilot validation study [16]. The BSDF measurement interpolation and subsequent interpolant sampling workflow performed well to conserve energy in the exiting BSDF hemisphere with some exceptions at grazing angles (Figs. 7-8). However, unlike the prior study, measured vertical illuminance and solar flux within an outgoing 2.5° cone ($L_{s,2.5°}$) were underpredicted (i.e., MBE error of −12.3% and −37.68%, respectively, with the tensor tree BSDF). Potential sources of error include those introduced by the BSDF generation workflow and to a lesser extent by field conditions such as differences in weave between the samples used in the laboratory versus field study, manufacturing variations across the sample used in the field test, positional errors with sensors, sensor and measurement errors, and errors between actual and modeled sky conditions.

Variations in weave due to manufacturing are potentially a source of random (across face of sample) or systematic error (distinct differences between small pgII and large field samples). The manufacturer was requested to cut the small pgII and large field test samples out of the same "batch" from the production line. However, variations still occurred. Data for one of the fabrics had

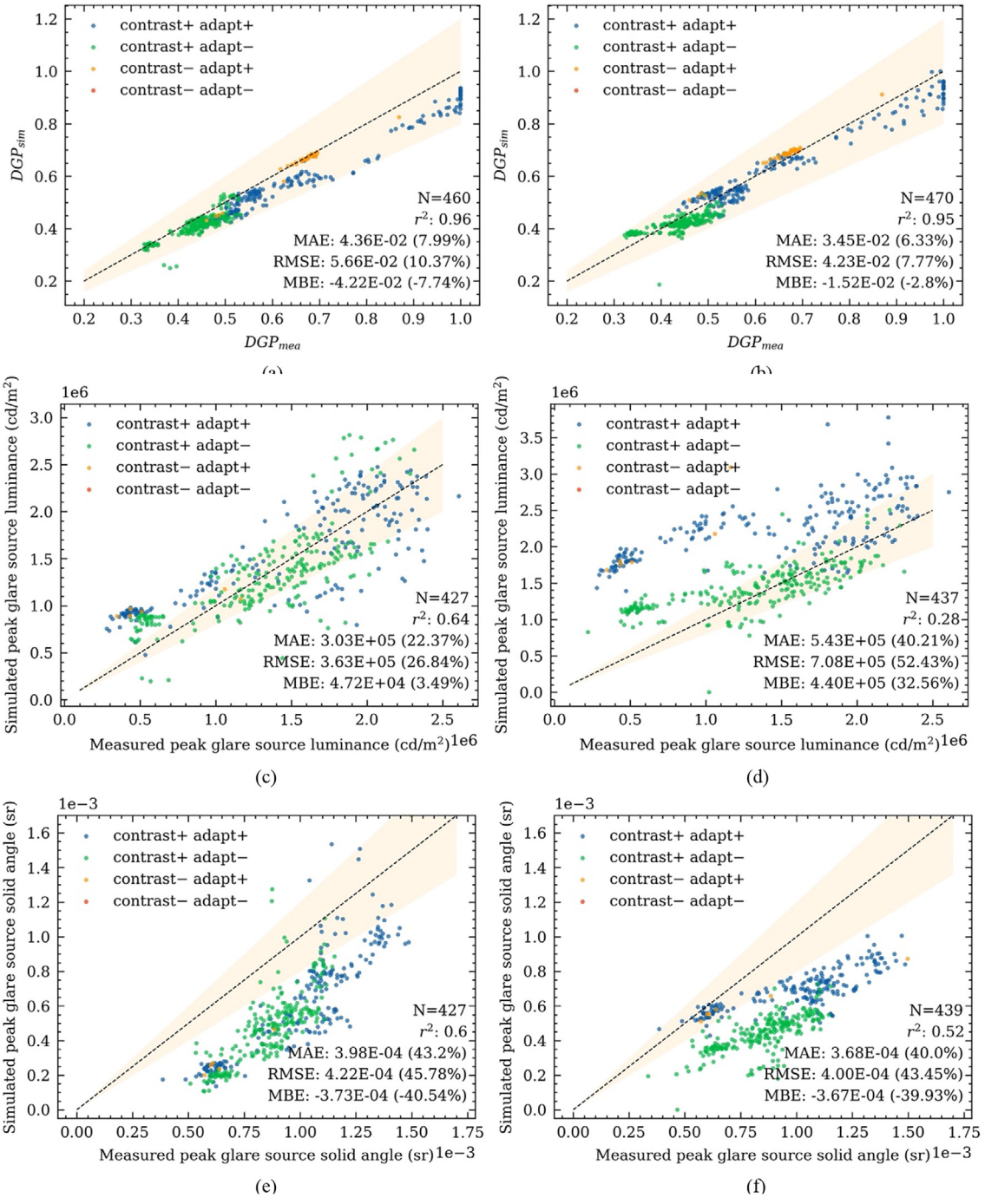

Fig. 11. Overall DGP (1st row), peak source (solar) luminance (cd/m^2, 2nd row) and solid angle (sr,3rd row), agreement between simulated (y-axis) and measured (x-axis) data where PE was fully triggered. DGP plots include BL1 dataset where PE is not turned on (BSDF material type was used instead of aBSDF), hence the larger dataset (N value). BL1 not included in $L_{s,e}$ or omega plots. Left: tensor tree; right: Klems dataset. The shaded area denotes an error range of ± 20%.

to be excluded due to unusually large differences between simulated and measured E_v data. A sample was cut out of the field test shade and measured, confirming that the E_v difference was due to differences in weave between the pgII and field test sample, i.e., $\tau_{v,\ n\text{-}h}$ of 0.021 versus 0.045, respectively. A systematic analysis between tested and lab measured samples should be done in future studies.

While the BSDF generation workflow also preserved transmission peaks, the peak shape and intensity were nevertheless reduced and spread out after interpolating individual measurement points into a series of gaussian lobes. The peaks were further reduced and spread out after sampling the gaussian lobes into a tabulated BSDF dataset (Fig. 14). As a result, of the eleven tested fabrics, BD1, with the lowest $\tau_{v,\ n\text{-}h}$ = 0.01 and $\tau_{v,\ n\text{-}n}$ = 0.007, failed to trigger peak extraction for all of its measured data points. The next least transmissive fabric, BD3 ($\tau_{v,\ n\text{-}h}$ = 0.028, $\tau_{v,\ n\text{-}n}$ = 0.025, failed to trigger peak extraction for some of its data points. All other fabrics fully triggered peak extraction for all measured data points. This phenomenon of spreading out the peak can potentially cause an underestimation of the tabulated BSDF peak, and, consequently, solar luminance as seen in Fig. 10.

To avoid identifying peaks that are not actually present, the BSDF peak resulting from the measurement, interpolation, and resampling workflow must be sufficiently pronounced. A system with low hemispherical and specular transmission is not likely to trigger peak

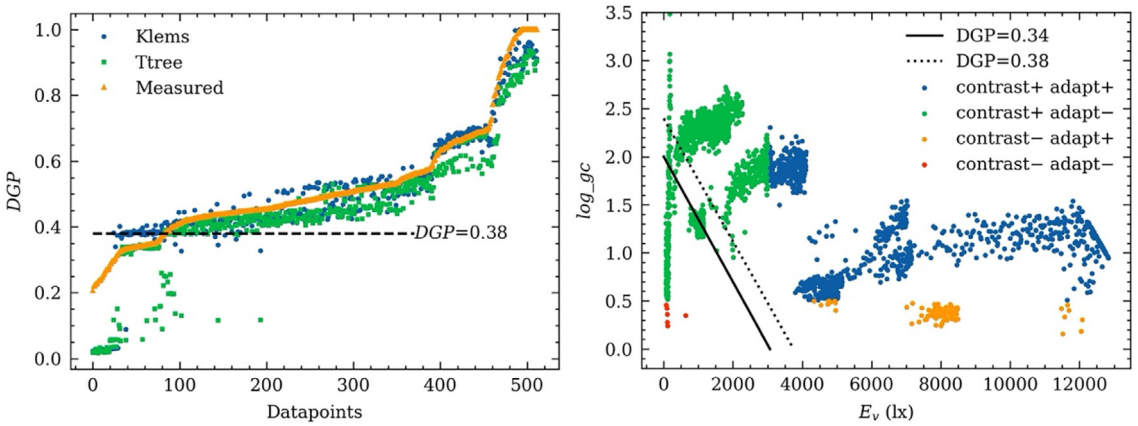

Fig. 12. Left: All measured and simulated (Klems and tensor tree dataset) DGP data points sorted by measured DGP in ascending order along the x-axis. Right: All measured vertical illuminance and log_gc conditions and their relationship to DGP = 0.34 and 0.38. E_v levels of 100–200 lx were due to the BD1 fabric.

extraction. For the simulated period, BD1 had a non-trivial amount of peak direct solar transmission through the fabric ($L_{s,e}$ = 1e5–3e5 cd/m^2) for the incident theta (30-35°) but failed to trigger PE. Without peak extraction, the resolution of the tensor tree representation (resolution of 4096 × 4096, 2.53° apex angle) was not high enough to resolve the solar disk, resulting in underestimation of solar luminance values.

When PE was triggered, simulated luminance values were significantly lower than measured values (i.e., Ls,2.5° MBE −3.46e5, −37.68%). Much of this error can be attributed to the reduction and spread of the peak across the BSDF generation workflow (Fig. 14) and potentially the variation between field and lab measured samples as discussed above. With *evalglare*, the compound effect of the workflow on peak shape and intensity (reflected in Ls) are separated: $L_{s,e}$ is now over-estimated (MBE of 4.84e4 cd/m^2, 3.58%) and the source solid angle is under-estimated (Fig. 11). Barring the effects of other sources of error, these PE error trends with L_s, $L_{s,e}$ and omega are the same irrespective of adaptation and contrast level or BSDF resolution. With the tensor tree basis, the diffuse scattering around the shoulder of the peak in the through direction is not extracted, whereas with Klems, the large patch includes more of the diffuse scattering and is included with the specular peak. This affects the magnitude of intensity between the two bases: there is significantly greater error in $L_{s,e}$ with the Klems basis compared to that of the tensor tree but near comparable errors with source solid angle.

Visual conditions involving contrast-based glare (E_v < 3000 lx) are heavily influenced by glare source size and intensity, so underestimations of these inputs will result in underestimated glare when using hybrid (e.g., DGP, predicted glare sensation vote (PGSV) [42], experimental unified glare rating (UGRexp) [43]) and contrast-based glare metrics (e.g., daylight glare index (DGI) [44], visual comfort probability [45]). For example, with BD1 where PE failed to trigger, MAE for Ls,2.5° was 2.64e4 cd/m^2 (87.1%). To address this issue, improvements to the interpolation and interpolation sampling algorithm are needed so that the peak's intensity and shape are better preserved. This would enable the PE algorithm to trigger more reliably. Alternatively, peaks can be extracted based on analytical models that are derived from the goniophotometer measurements.

Separately, among cases where PE was triggered, analysis of E_v, L_s, and DGP errors did not reveal clear trends with general material characteristics (e.g., $\tau_{v,\ n\text{-}n}$ and $\tau_{v,\ n\text{-}h}$). Errors varied considerably across the measured angles of incidence due to the complex scattering, specular, and near specular transmission behavior of the anisotropic fabrics and were influenced in part by the local conditions of each sample in the field study.

4.2. Effect of workflow errors on DGP results

Results in Section 3.3 verified that the workflow and PE method can predict binary glare/ no-glare with a true positive rate and true negative rate of 0.98 and 1.0 when the tensor tree BSDF dataset was used. The Klems dataset produced significantly less accuracy in predicting binary glare discomfort, especially when predicting no-glare cases.

The overall DGP MAE across all eleven fabrics was 0.063 (11%), with errors for individual fabric ranging from 0.007 to 0.100. When PE was not used for fabric that doesn't have distinct through component (BL1), L_s error was less relevant due to lack of specular transmission: the E_v and DGP errors were minimal with a MAE of 85 lx (1.06%) and 0.0048 (0.71%), respectively. For cases where PE (i.e., aBSDF) was specified but failed to trigger due to reasons mentioned in Section 4.1, DGP MAE approached 80% due to significantly underpredicted source luminance. In cases where PE was triggered, DGP MAE was 0.044 (8.0%).

The significance of simulation errors per adaptation and contrast categories is illustrated in Fig. 15:

- For E_v greater than 3000 lx (high adaptation), DGP increases linearly with E_v (high adaptation, saturation discomfort glare) with almost all DGP values in the range of intolerable glare (greater than0.45). In this range, an E_v MAE of 810 lx (11.9%) is likely to be of sufficient accuracy and a DGP MBE of −0.07 of minor to no consequence.
- For E_v < 3000 lx (low adaptation), DGP was at or above the 0.38 borderline between noticeable and disturbing (BND) glare with $L_{s,e}$ greater than or equal to 7.5e5 cd/m^2 (green to yellow on false-color scale). DGP was at or above the 0.45 borderline between disturbing and intolerable (BDI) for $L_{s,e}$ greater than or equal to 1.2e6 cd/m^2 (yellow to red). Here, a DGP MAE of 0.0293 corresponds to about half a point in the four-point glare rating scale.

For scenarios with E_v<3000 lx, the measurement, interpolation, and PE workflow may be of insufficient accuracy to evaluate borderline performance between fabrics (e.g., EN 17,037 DGP_e < 5% for glare protection thresholds of DGP = 0.35, 0.40, or 0.45), particularly under low adaptation, high contrast conditions.

Note that there are inherent uncertainties associated with discomfort glare metrics, since there is considerable variation in subjective response in response to daylit conditions. Future effort should focus on the improving prediction accuracy of source luminance in low adaptation conditions because discomfort glare is more sensitive to source luminance contrast than vertical illuminance at the eye. Errors associated with *evalglare* detected source

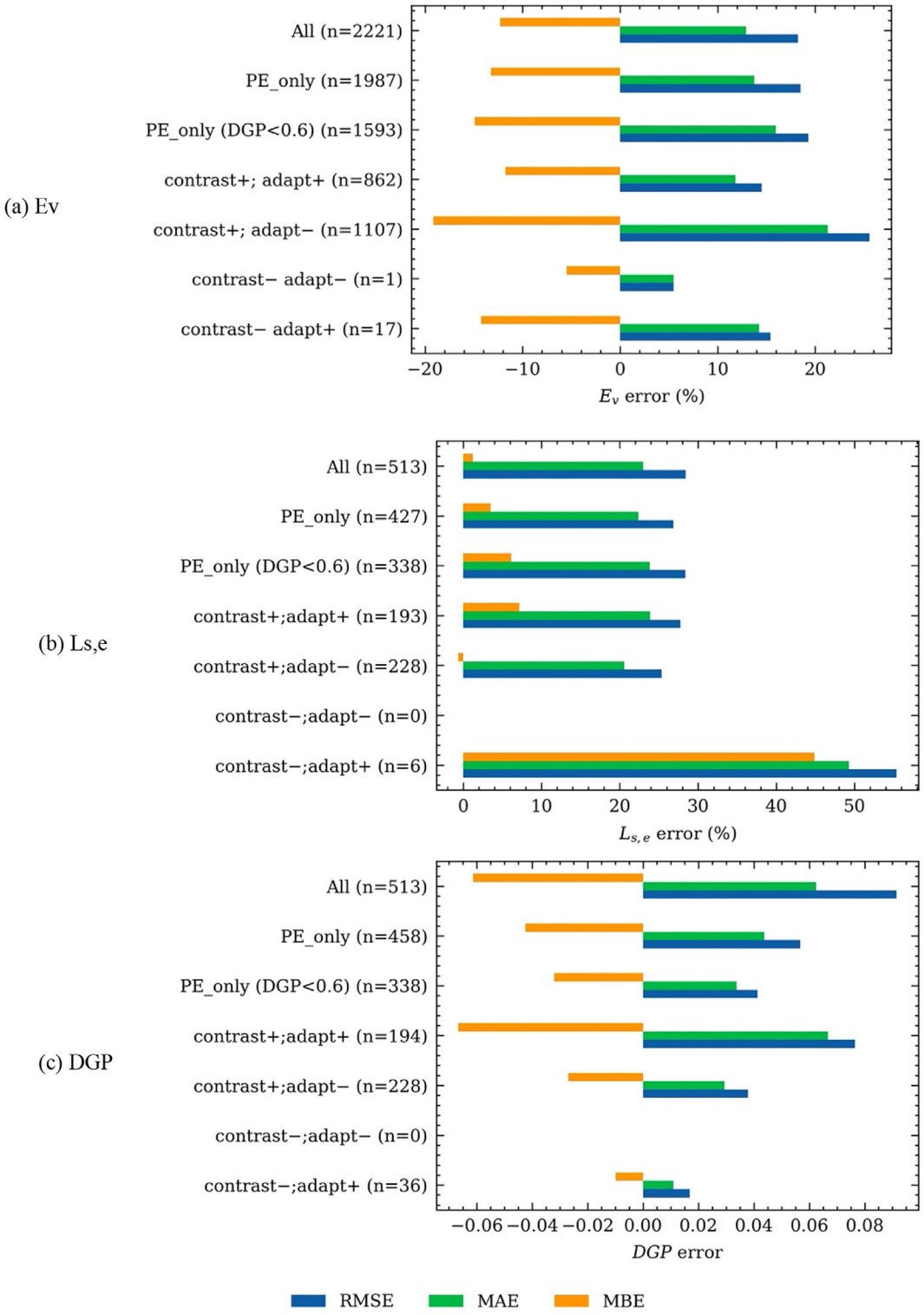

Fig. 13. a) Vertical illuminance (E_v) error (%), simulated at a 1 min interval using *rtrace*, b) peak source luminance ($L_{s,e}$) error (%), and (c) DGP absolute error, where $L_{s,e}$ and DGP were derived from HDR images captured at a 10 min interval. Upper three datasets per chart: All data, data where PE was triggered, and data where PE was triggered and DGP < 0.6. Lower four datasets per chart: All data where PE was triggered sorted by the four contrast and adaptation categories. Tensor tree BSDF datasets only.

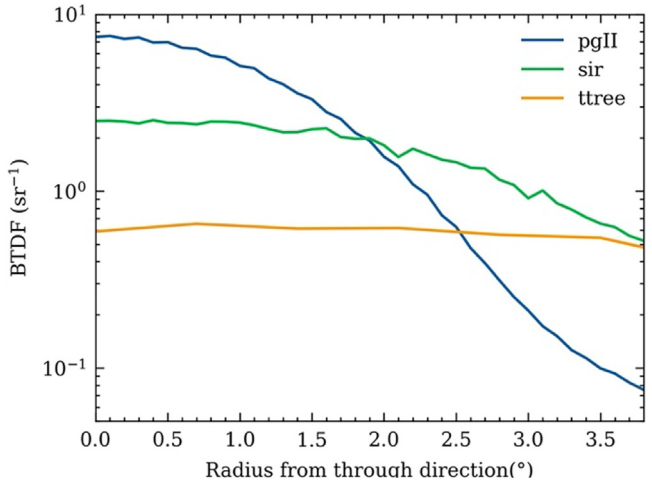

Fig. 14. BTDF near the through direction for BD1 fabric evaluated from raw measurement data (pgll), intermediate scattering interpolant representation (sir), and final tabulated BSDF data (ttree), with incident theta = 30° and phi = 90°.

solid angle will likely improve as a result (due to larger amount of pixel blurred specular peak > 5e4 cd/m^2). Analysis of the significance of these errors should be extended to other glare metrics (e.g., DGI, UGR) when algorithms for source detection have been further developed and validated.[5] There may also be differences in interpretation of what constitutes a glare source. In the case of [46], the *evalglare* peak extraction algorithm was turned off so that the solar disk and circumsolar region were merged, resulting in a much larger and less intensive glare source. In recent work [47], researchers indicated that modifications to glare calculation methods were underway with updates planned for early 2022.

4.3. Applicability

We used a broad range of fabrics for this field validation study with the intention to encompass the variable specular, near specular, and scattering behavior of all shading and daylighting materials with an effective "view" component. Uncertainty due to manufacturing variations in fabric shade materials however limits the outcomes from this study to woven fabrics. Errors may be lower for shading materials that do not exhibit such manufactured variability.

As indicated in [16] and [33], alternate simulation methods may be recommended for other types of systems. This workflow, for example, would not be applicable to systems with "near-specular" transmission such that it defocuses the view, such as lightly-etched glass. In such cases, PE should not be used as it would cause significant overestimation of glare. For macroscopic systems that can be represented with geometry, such as louvers and venetian blinds, proxy geometry should be used to model specular transmission between the slats of the blinds. In cases where geometry is not available, PE should be used with such systems to make sure the specular peak is properly modeled. Other systems such as prismatic systems with multiple specular transmission directions would require very high measurement resolution and intensive sampling to get reasonable accuracy; such systems should also not be modeled with PE.

Guidance on how to model systems in terms of speed and accuracy tradeoffs were also provided in the prior validation study [16]. If the material is anisotropic and only laterally symmetric, then assuming that the material is isotropic when measuring the scattering properties of the material can lead to significant errors. Even though, in some cases (e.g., $L_{s,e}$), Klems dataset performed better in terms of absolute error, r^2 values were across the board lower than that of tensor tree datasets', indicating an inferior correlation to the measurement. This can be largely blamed on the fixed low resolution from the Klems basis.

A tensor tree resolution of 4096 × 4096 as was used in this study provides a practical balance between speed and accuracy, given today's computational limits. Observation of view through a material at normal incidence and at arm's length was used to determine whether or not to specify the *aBSDF* material type to invoke PE.

5. Conclusions

Illuminance, luminance, and discomfort glare were simulated for eleven fabrics representing a broad range of forward scattering, specular transmitting materials and validated against field measurements in a full-scale outdoor testbed. Data-driven methods of interpolating goniophotometer measurements and subsequent interpolant sampling were shown to conserve energy over the BSDF exiting hemispheres. As a result, simulated vertical illuminance agreed well with field measurements, which is critical for predicting discomfort glare in high adaptation cases. Ten of the eleven fabrics were simulated with peak extraction, where PE triggered fully in eight fabrics with strong specular transmission, while one (BD3) triggered PE in most cases and another (BD1) failed completely due to reasons explained in Section 4. Of the cases where PE was triggered fully, *evalglare*-extracted source luminance agreed well enough between simulated and measured values to predict binary glare/ no-glare discomfort (DGP greater than 0.38) with near perfect accuracy with the tensor tree BSDF dataset but was not of sufficient accuracy to distinguish between glare levels on the four-point scale, particularly in cases of low adaptation, high contrast glare. Anisotropic Klems BSDF datasets may be sufficient for predicting binary glare in high adaptation scenarios. Designers and engineers can rely on data-driven tabulated BSDF datasets produced using the workflow described in this paper to predict energy and non-energy (i.e., binary-scale visual comfort) performance of fabric shading systems. Errors may be lower for other types of shading materials that do not exhibit the variability in weave that occur with manufactured fabrics. Future research should be directed to improving measurement interpolation and interpolant sampling algorithms to better preserve measurement fidelity, which will also improve PE performance. Alternatively, analytical models for predicting direct-direct transmission for certain types of systems may also provide better glare luminance prediction for low adaptation, high contrast scenarios.

Declaration of Competing Interest

The authors declare that they have no known competing financial interests or personal relationships that could have appeared to influence the work reported in this paper.

Acknowledgments

This work was supported by the Assistant Secretary for Energy Efficiency and Renewable Energy, Building Technologies Office of the US Department of Energy under Contract No. DE-AC02-05CH11231. In-kind support for shade materials was provided by Mechoshade, Inc. Scanning-goniophotometer measurements were performed by Lars O. Grobe at the Lucerne University of Applied Sciences and Arts (HSLU), Switzerland. Peak extraction algorithm development and debugging was supported by David Geisler-Moroder at Bartenbach GmbH.

[5] There are algorithm uncertainties around how the solar peak gets extracted from the HDR image, i.e., what is considered a solar glare source. Existing research has been focusing on DGP, with methods of the extracting the solar peak established against occupants' subjective response data. Future research is needed to establish similar methods for other glare metrics.

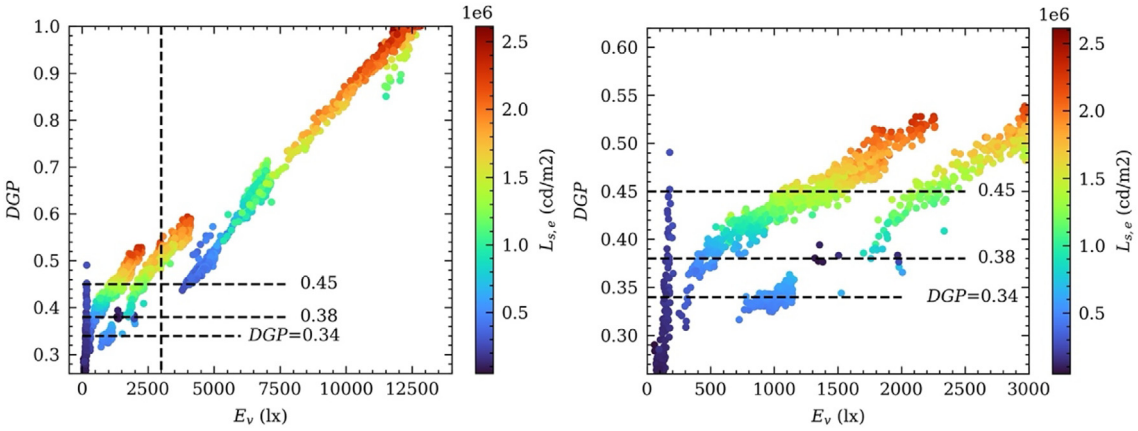

Fig. 15. Left: Vertical illuminance (lx) versus measured DGP for conditions when PE was fully triggered with tensor tree data. Right: Expanded view for contrast glare conditions (E_v < 3000 lx). Measurement conditions: $L_{s,e}$ = 3e5–2.6e6 cd/m^2, position index = 3–4, source solid angle = 5e-4 to 1.5e-3 sr.

Appendix A

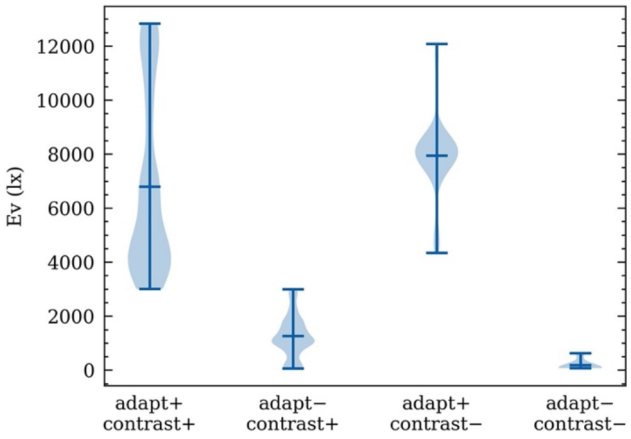

Fig. A1. Violin plot showing measured vertical illuminance distribution for four adaptation and contrast conditions. Ticks indicate extremes and mean.

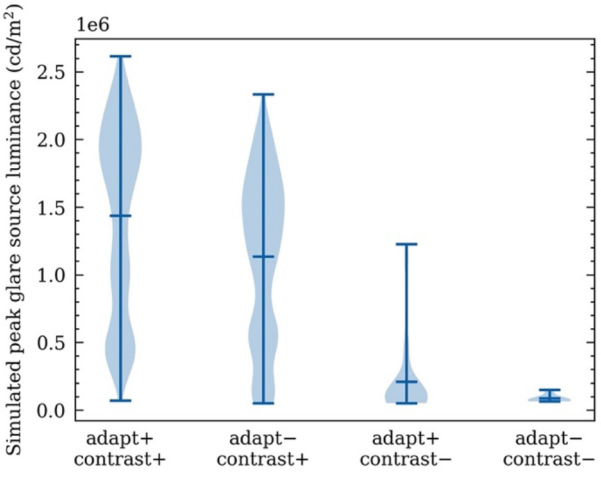

Fig. A2. Violin plot showing measured solar luminance distribution evaluated at 2.5° cone for four adaption and contrast conditions. Ticks indicate extremes and mean.

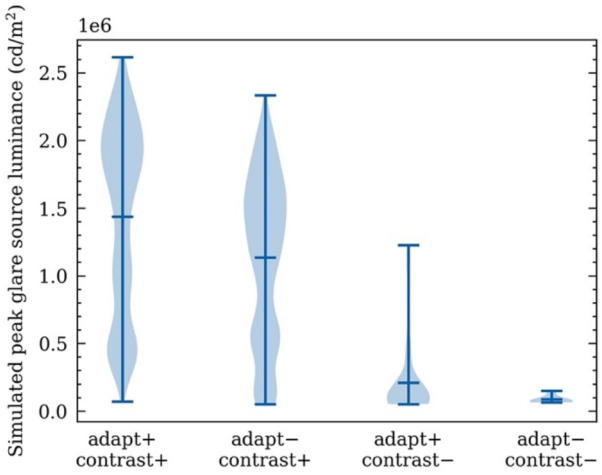

Fig. A3. Violin plot showing measured solar luminance extracted from *evalglare* for four adaption and contrast conditions. Ticks indicate extremes and mean.

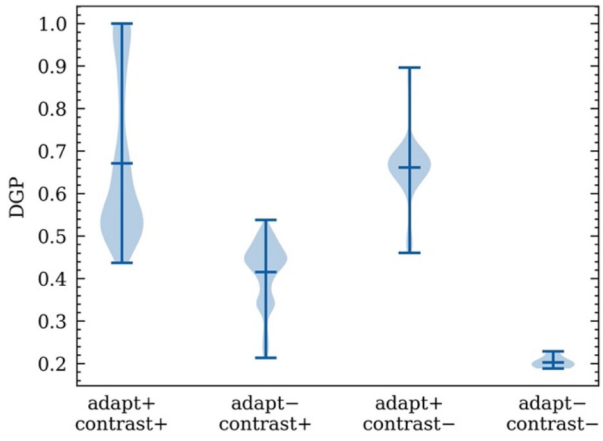

Fig. A4. Violin plot showing measured DGP for four adaption and contrast conditions. Ticks indicate extremes and mean.

Table A1
Ev (lx) error: Tensor tree.

	Data count	r^2	RMSE	nRMSE(%)	MAE	nMAE(%)	MBE	nMBE(%)
All	2,221	0.99	675.7	18.2	478.1	12.9	−455.5	−12.3
PE_only	2,053	0.99	702.7	17.5	515.7	12.8	−492.0	−12.3
PE_only (DGP < 0.6)	1,593	0.96	437.6	19.3	361.6	16.0	−337.7	−14.9
contrast+;adapt+	863	0.99	985.8	14.5	804.7	11.8	−797.9	−11.7
contrast+;adapt−	1,107	0.83	370.8	25.6	308.5	21.3	−277.7	−19.2
contrast−;adapt−	1	n/a	34.5	5.5	34.5	5.5	−34.5	−5.5
contrast−;adapt+	82	0.92	529.5	6.7	278.1	3.5	−169.2	−2.1

Table A2
Ev error: Klems.

	Data count	r^2	RMSE	nRMSE(%)	MAE	nMAE(%)	MBE	nMBE(%)
All	2,221	0.99	531.8	14.4	373.4	10.1	−307.1	−8.3
PE_only	2,061	0.98	551.8	13.8	399.6	10	−332.5	−8.3
PE_only (DGP < 0.6)	1,601	0.97	376.6	16.7	301.6	13.4	−269.8	−11.9
contrast+;adapt+	863	0.98	704.1	10.4	498.8	7.3	−438.5	−6.4
contrast+;adapt−	1,115	0.82	401.7	27.8	319.3	22.1	−291.9	−20.2
contrast−;adapt−	1	n/a	84.6	13.4	84.6	13.4	84.6	13.4
contrast−;adapt+	82	0.95	491.6	6.2	451.1	5.7	226.5	2.8

Table A3
Evalglare extracted peak glare source luminance error: tensor tree.

	Data count	r^2	RMSE	nRMSE(%)	MAE	nMAE(%)	MBE	nMBE(%)
All	513	0.77	344,814.7	28.4	278,769.1	23	14,753.3	1.2
PE_only	427	0.64	363,140.8	26.8	302,541.3	22.4	47,242.4	3.5
PE_only (DGP < 0.6)	338	0.64	358,269.1	28.4	300,705	23.8	77,543.9	6.2
contrast+;adapt+	193	0.69	399,233.7	27.7	343,885.8	23.9	103,681.4	7.2
contrast+;adapt−	228	0.59	328,278.2	25.4	266,060.5	20.6	−7,895.4	−0.6
contrast−;adapt−	0	n/a	n/a	n/a	n/a	n/a	n/a	n/a
contrast−;adapt+	6	0.82	403,413.6	55.4	358,897.5	49.2	327,028.4	44.9

Table A4
Evalglare extracted peak glare source luminance: Klems.

	Data count	r^2	RMSE	nRMSE(%)	MAE	nMAE(%)	MBE	nMBE(%)
All	515	0.54	662,979.5	54.7	492,876	40.6	383,768.9	31.6
PE_only	437	0.28	707,880.6	52.4	542,837.5	40.2	439,638.4	32.6
PE_only (DGP < 0.6)	348	0.23	624,717.5	49.6	466,799.2	37.1	339,646.6	27
contrast+;adapt+	193	0.45	951,541.3	66.1	818,323.5	56.9	801,091.5	55.7
contrast+;adapt−	238	0.53	368,225.9	28.6	298,112.1	23.1	122,598.5	9.5
contrast−;adapt−	0	n/a	n/a	n/a	n/a	n/a	n/a	n/a
contrast−;adapt+	6	0.79	1,411,847	193.8	1,388,815	190.6	1,388,815	190.6

Table A5
Evalglare extracted peak glare source solid angle: tensor tree.

	Data count	r^2	RMSE	nRMSE(%)	MAE	nMAE(%)	MBE	nMBE(%)
All	513	0.04	0.251899	30108.39	0.023316	2786.92	0.022665	2709.1
PE_only	427	0.6	0.000422	45.8	0.000398	43.2	−0.000370	−40.5
PE_only (DGP < 0.6)	338	0.54	0.000413	48.4	0.000389	45.6	−0.000360	−42.4
contrast+;adapt+	193	0.64	0.000422	41.6	0.000396	39.1	−0.000375	−36.5
contrast+;adapt−	228	0.44	0.000423	50.0	0.000401	47.3	−0.000386	−44.7
contrast−;adapt−	0	n/a	n/a	n/a	n/a	n/a	n/a	n/a
contrast−;adapt+	6	0.97	0.000354	37.2	0.000347	36.5	−0.000284	−29.4

Table A6
Evalglare extracted peak glare source solid angle: Klems.

	Data count	r^2	RMSE	nRMSE(%)	MAE	nMAE(%)	MBE	nMBE(%)
All	515	0.13	0.553005	66098.3	0.107151	12,807.3	0.106509	12730.6
PE_only	437	0.52	0.000400	43.5	0.000368	40.0	−0.000374	−40.0
PE_only (DGP < 0.6)	348	0.3	0.000396	46.5	0.000362	42.5	−0.000360	−42.4
contrast+;adapt+	193	0.65	0.000367	36.2	0.000320	31.6	−0.000322	−31.4
contrast+;adapt−	238	0.5	0.000427	50.6	0.000412	48.7	−0.000411	−48.7
contrast−;adapt−	0	n/a	n/a	n/a	n/a	n/a	n/a	n/a
contrast−;adapt+	6	0.99	0.000276	29.0	0.00018	18.9	−0.000180	−18.9

Table A7
DGP error: tensor tree.

	Data count	r^2	RMSE	nRMSE(%)	MAE	nMAE(%)	MBE	nMBE(%)
All	513	0.87	0.092	17.4	0.063	11.9	−0.061	−11.7
PE_only	458	0.96	0.057	10.4	0.044	8.0	−0.042	−7.8
PE_only (DGP < 0.6)	338	0.82	0.041	8.9	0.034	7.3	−0.032	−6.9
contrast+;adapt+	194	0.97	0.077	11.4	0.067	9.9	−0.067	−9.9
contrast+;adapt−	228	0.75	0.038	8.7	0.029	6.7	−0.027	−6.2
contrast−;adapt−	0	n/a	n/a	n/a	n/a	n/a	n/a	n/a
contrast−;adapt+	36	0.97	0.017	2.5	0.011	1.6	−0.010	−1.5

Table A8
DGP error: Klems.

	Data count	r^2	RMSE	nRMSE(%)	MAE	nMAE(%)	MBE	nMBE(%)
All	515	0.89	0.069	13.1	0.046	8.7	−0.026	−5.0
PE_only	468	0.95	0.042	7.8	0.034	6.3	−0.015	−2.8
PE_only (DGP < 0.6)	348	0.69	0.039	8.4	0.033	7.1	−0.013	−2.7
contrast+;adapt+	194	0.96	0.047	7.0	0.037	5.6	−0.020	−2.9
contrast+;adapt−	238	0.64	0.040	9.3	0.034	7.9	−0.017	−4.0
contrast−;adapt−	0	n/a	n/a	n/a	n/a	n/a	n/a	n/a
contrast−;adapt+	36	0.98	0.024	3.6	0.020	3.1	0.020	3.1

References

[1] G. Mbise, G.B. Smith, G.A. Niklasson, C.G. Granqvist, Angular selective window coatings: theory and experiment, SPIE Proc. (1989).
[2] G.B. Smith, C.-G.-S. Granqvist, Green Nanotechnology, CRC Press, 2010.
[3] T. Wang, G. Ward, E.S. Lee, Efficient modeling of optically-complex, non-coplanar exterior shading: validation of matrix algebraic methods, Energy Build. 174 (2018) 464–483.
[4] S. Hoffmann, E.S. Lee, A. McNeil, L. Fernandes, D. Vidanovic, A. Thanachareonkit, Balancing daylight, glare, and energy-efficiency goals: an evaluation of exterior coplanar shading systems using complex fenestration modeling tools, Energy Build. 112 (2016) 279–298.
[5] L.L. Fernandes, E.S. Lee, A. McNeil, J.C. Jonsson, T. Nouidui, X. Pang, S. Hoffmann, Angular selective window systems: assessment of technical potential for energy savings, Energy Build. 90 (2015) 188–206.
[6] Commission Internationale De L'Eclairage, "Ocular lighting effects on human physiology and behaviour," 2004.
[7] M.H. Smolensky, L.L. Sackett-Lundeen, F. Portaluppi, Nocturnal light pollution and underexposure to daytime sunlight: complementary mechanisms of circadian disruption and related diseases, Chronobiol. Int. 32 (2015) 1029–1048.
[8] F. E. Nicodemus, J. C. Richmond, J. J. Hsia, I. W. Ginsberg and T. Limperis, "Geometrical Considerations and Nomenclature for Reflectance," in *Radiometry*, USA, Jones and Bartlett Publishers, Inc., 1992, p. 94–145.
[9] P. Apian-Bennewitz, Design and Construction of a Device for Measuring Light-Scattering on Anisotropic Materials, 2021.
[10] J.H. Klems, A new method for predicting the solar heat gain of complex fenestration systems I. Overview and derivation of the matrix layer calculation, ASHRAE Trans. 100 (1994).
[11] M. Andersen, J. de Boer, Goniophotometry and assessment of bidirectional photometric properties of complex fenestration systems, Energy Build. 38 (7) (2006) 836–848.
[12] Attachements Energy Rating Council, "AERC 1.1: Procedures for Determining the Optical and Thermal Properties of Window Attachment Materials," v1.3, 2018b, Appendix C, Available: https://aercnet.org/product/aerc-1-1-procedures-determining-optical-thermal-properties-window-attachment-materials/. [Accessed 15 9 2021].
[13] "Euporean Solar Shading Organisation (ES-SO)," [Online]. Available: https://es-so.com. [Accessed 24 9 2021].
[14] J. Stover, Optical scattering: measurement and analysis, SPIE Optical Engineering Press, Bellingham, Wash., USA, 1995.
[15] A. McNeil, J. Jonsson, D. Appelfeld, G. Ward, E.S. Lee, A validation of a ray-tracing tool used to generate bi-directional scattering distribution functions for complex fenestration systems, Sol. Energy 98 (2013) 404–414.
[16] G.J. Ward, T. Wang, D. Geisler-Moroder, E.S. Lee, L.O. Grobe, J. Wienold, J.C. Jonsson, Modeling specular transmission of complex fenestration systems with data-driven BSDFs, Build. Environ. 196 (2021) 107774.
[17] M. Andersen, L. Michel, C. Roecker, J.-L. Scartezzini, Experimental assessment of bi-directional transmission distribution functions using digital imaging techniques, Energy Build. 33 (5) (2001) 417–431.
[18] G. Larson, R. Shakespear, Rendering with radiance: The art and science of lighting visualization, San, Morgan Kaufmann Publishers, Francisco, 1998.
[19] P.R. Tregenza, I.M. Waters, Daylight coefficients, Light. Res. Technol. 15 (2) (1983) 65–71.
[20] J. Mardaljevic, Simulation of annual daylighting profiles for internal illuminance, Light. Res. Technol. 32 (3) (2000) 111–118.
[21] C.F. Reinhart, S. Herkel, The simulation of annual daylight illuminance distributions — a state-of-the-art comparison of six RADIANCE-based methods, Energy Build. 32 (2) (2000) 167–187.
[22] C.F. Reinhart, O. Walkenhorst, Validation of dynamic RADIANCE-based daylight simulations for a test office with external blinds, Energy Build. 33 (7) (2001) 683–697.
[23] M. Saxena, G. Ward, T. Perry, L. Heschong and R. Higa, "Dynamic Radiance - Predicting annual daylighting with variable fenestration optics using BSDFs," *Fourth National Conference of IBPSA-USA*, January 2010.
[24] G. Ward, R. Mistrick, E.S. Lee, A. McNeil, J. Jonsson, Simulating the daylight performance of complex fenestration systems using bidirectional scattering distribution functions within radiance, LEUKOS 7 (4) (2011) 241–261.
[25] N.A. Kotey, J.L. Wright, M.R. Collins, Determining off-normal solar optical properties of roller blinds, ASHRAE Trans. (2009).
[26] J. Wienold, T. Kuhn, J. Christoffersen and M. Andersen, "Annual glare evaluation for fabrics," Proceedings PLEA 2017, Edinburgh, July 3-5, 2017. Additional material: https://infoscience.epfl.ch/record/231231
[27] A. McNeil, "On the sensitivity of daylight simulations to the resolution of the hemispherical basis used to define bidirectional scattering distribution functions," DOE/LBNL FY11 Technical Report, 2011.
[28] A. McNeil, "The Five-Phase Method for Simulating Complex Fenestration with Radiance," Available: https://facades.lbl.gov/sites/all/files/tutorial-fivephasemethod.pdf, 2013 [Accessed 15 9 2021]
[29] D. Geisler-Moroder, E.S. Lee, G.J. Ward, Validation of the Five-Phase Method for Simulating Complex Fenestration Systems with Radiance against Field Measurements, in 15th International Conference of the International Building Performance Simulation Association, 2017.
[30] E. Brembilla, D.A. Chi, C.J. Hopfe, J. Mardaljevic, Evaluation of climate-based daylighting techniques for complex fenestration and shading systems, Energy Build. 203 (2019) 109454.
[31] E.S. Lee, D. Geisler-Moroder, G. Ward, Modeling the direct sun component in buildings using matrix algebraic approaches: methods and validation, Sol. Energy 160 (2018) 380–395.
[32] L.O. Grobe, Photon-mapping in climate-based daylight modelling with high-resolution BSDFs, Energy Build. 205 (2019) 109524.
[33] D. Geisler-Moroder, G.J. Ward, T. Wang, E.S. Lee, Peak extraction in daylight simulations using BSDF data, Proceedings of Building Simulation 2021, 2021.
[34] P. Apian-Bennewitz, J. von der Hardt, Enhancing and calibrating a goniophotometer, Sol. Energy Mater. Sol. Cells 54 (1-4) (1998) 309–322.
[35] L.O. Grobe, S. Wittkopf, P. Apian-Bennewitz, J.C. Jonsson, M. Rubin, Experimental validation of bidirectional reflection and transmission distribution measurements of specular and scattering materials, SPIE Proc. (2010).
[36] D. Geisler-Moroder, P. Apian-Bennewitz, J. de Boer, B. Bueno, B. Deroisy, Y. Fang, L. O. Grobe, J. C. Jonsson, E. S. Lee, Z. Tian, T. Wang, G. J. Ward, H. R. Wilson and Y. Wu, "Analysis and evaluation of BSDF characterization of daylighting systems," T61.C.2.2 – A Technical Report of Subtask C, IEA SHC Task 61 / EBC Annex 77, Available: https://task61.iea-shc.org/publications, 2021 [Accessed 15 9 2021]
[37] G. Ward, M. Kurt and N. Bonneel, "A Practical Framework for Sharing and Rendering Real-World Bidirectional Scattering Distribution Functions," LBNL 5954E, Lawrence Berkeley National Laboratory, Berkeley, CA, September 2012.
[38] J. Wienold, "Evalglare version 2.0," in *Radiance Workshop*, Padua, 2016.
[39] J. Wienold, J. Christoffersen, Evaluation methods and development of a new glare prediction model for daylight environments with the use of CCD cameras, Energy Build. 38 (7) (2006) 743–757.

[40] G. Quek, J. Wienold, M.S. Khanie, E. Erell, E. Kaftan, A. Tzempelikos, I. Konstantzos, J. Christoffersen, T. Kuhn, M. Andersen, Comparing performance of discomfort glare metrics in high and low adaptation levels, Build. Environ. 206 (2021) 108335.
[41] G. Quek, S. Wasilewski, J. Wienold, M. Andersen, Spatial evaluation of potential saturation and contrast effects of discomfort glare in an open-plan office, Build. Simul. (2021).
[42] M. Tokura, T. Iwata, M. Shukuya, Experimental study on discomfort glare caused by windows part 3: development of a method for evaluating discomfort glare from a large light source, J. Archit. Plann. (Trans. AIJ) 61 (489) (1996) 17–25.
[43] K. Fisekis, M. Davies, M. Kolokotroni, P. Langford, Prediction of discomfort glare from windows, Light. Res. Technol. 35 (4) (2003) 360–369.
[44] R.G. Hopkinson, Glare from daylighting in buildings, Appl. Ergon. 3 (4) (1972) 206–215.
[45] M. S. Rea, The IESNA Lighting Handbook: Reference & Application, Illuminating Engineering Society of North America, 2000.
[46] S. Jain, C. Karmann, J. Wienold, Behind electrochromic glazing: assessing user \textquotesingles perception of glare from the sun in a controlled environment, Energy Build. 256 (2022) 111738.
[47] S. Jain and J. Wienold, "Glare from the sun behind electrochromic glazing," in *Radiance Workshop*, Bilbao, Spain, 2021.
[48] W.K.E. Osterhaus, I.L. Bailey, Large area glare sources and their effect on visual discomfort and visual performance at computer workstations, in Conference Record of the 1992 IEEE Industry Applications Society Annual Meeting, 1992.